A highly reversible dendrite-free Zn anode via spontaneous galvanic replacement reaction for advanced zinc-iodine batteries

Yadong Tian[1], Song Chen[1], Yulong He[1], Qianwu Chen[1], Lili Zhang[2] (✉), and Jintao Zhang[1] (✉)

[1] Key Laboratory for Colloid and Interface Chemistry, Ministry of Education, School of Chemistry and Chemical Engineering, Shandong University, Jinan 250100, China

[2] Institute of Sustainability for Chemicals, Energy and Environment, Agency for Science, Technology and Research (A*STAR), 1 Pesek Road, Jurong Island 627833, Singapore

ABSTRACT

Rechargeable aqueous zinc-iodine batteries have received extensive attention due to their inherent advantages such as low cost, flame retardancy and safety. To address the safety concern associated with Zn dendrites, tin functional layer is introduced to the Zn surface via a spontaneous galvanic replacement reaction. This provides rapid deposition kinetics, thereby achieving the uniform Zn plating/stripping with a low overpotential (13.9 mV) and good stability for over 900 h. Importantly, the coupling of the advanced Zn anode with iodine in Zn-I$_2$ battery exhibits a high specific capacity of 196.4 mAh·g^{-1} with high capacity retention (90.7%). This work provides a reliable strategy to regulate the reversible redox of zinc for advanced rechargeable batteries.

KEYWORDS

tin, overpotential, induced deposition effect, Zn-I$_2$ batteries

1 Introduction

Energy crisis and increasing environmental concerns have urged people to look for alternative renewable clean energy and new technological solutions [1]. Lithium-based energy solutions represented by lithium-ion batteries face challenges such as high flammability, limited availability and high cost [2, 3]. Aqueous Zn-based batteries including Zn-I$_2$ batteries have received tremendous attention because of their inherent advantages (e.g., high theoretical specific capacity of 820 mAh·g^{-1}) and abundant reserves (earth crust Zn content of 0.0075% and 55 μg$_{iodine}$·L^{-1} in ocean) [4–15]. Nevertheless, the growth of Zn dendrites leads to battery failure and short-circuit due to the non-uniform deposition, resulting in the short lifespan of Zn-based batteries [16–18]. Additionally, the corrosion of Zn in aqueous electrolytes with the formation of undesirable byproducts (e.g., Zn$_4$SO$_4$(OH)$_6$·3H$_2$O) would inevitably result in the irreversible Zn plating/stripping process [19–22]. The insulating corrosion products on the surface of Zn can reduce the utilization efficiency of Zn and further increase the charge transfer resistance of the batteries. Besides, the continuous evolution of H$_2$ owing to a lower potential of Zn/Zn^{2+} (−0.76 V vs SHE) than that of H$_2$/H$^+$ (0 V vs. SHE) would increase the internal pressure and cause safety concern [23]. In this regard, the key of the development of high-performance Zn-based batteries is to reduce corrosion reaction and prevent the growth of Zn dendrites.

Therefore, a variety of advanced strategies have been developed to address the above challenges, which mainly focus on electrode interface modification [24–27], electrolyte regulation [28–30], and others. For instance, the anti-corrosion technology was combined to prepare a dendrite-free Zn anode by coating a dual-functional indium (In) layer on the Zn anode [22]. As both a corrosion inhibitor and nucleating agent, the bifunctional In coating greatly inhibited the corrosion and induced the uniform deposition to eliminate Zn dendrites. Such interface modification and coating technologies are efficient to reduce anodic corrosion and dendrite growth. Additionally, various additives (e.g., dimethyl sulfoxide) were introduced to inhibit the formation of irreversible products along with the water reduction [31]. The formation of solid electrolyte interphase (SEI) due to the decomposition of electrolytes would possibly prevent the formation of Zn dendrites. However, the presence of additives would enhance the polarization of Zn plating/stripping process and deteriorate the reversibility of zinc redox reactions. Therefore, it is still challenging to develop a highly reversible, dendrite-free and stable Zn anode.

Metal tin (Sn) possesses a high hydrogen evolution overpotential, chemical inertness, low cost and high adsorption energy for Zn, which is an ideal candidate as the coating material for Zn anode. Considering the congenital advantage of Sn and the good compatibility with Zn, a simple yet effective strategy is demonstrated to construct a highly reversible

Address correspondence to Jintao Zhang, jtzhang@sdu.edu.cn; Lili Zhang, zhang_lili@isce2.a-star.edu.sg

dendrite-free Zn anode via the formation of tin coating by the means of spontaneous displacement reaction. The Sn coating layer not only benefits the highly reversible Zn plating/stripping processes owing to the enhanced interaction of Sn with Zn, but also suppresses the occurrence of side reactions due to its inherent chemical inertness and isolation effect [32, 33]. Furthermore, the Sn coating layer provides proper nucleation sites and thereby greatly reduces the redox overpotential, enabling the uniform Zn deposition without dendrites. As expected, the as-prepared Zn|Sn anode exhibited an ultra-low redox overpotential (13.9 mV), only half of that for the bare Zn electrode (21.4 mV) and good cycling stabilities without obvious decay over 900 h. More importantly, the optimized Zn|Sn electrode was coupled with an iodine electrode to achieve a large specific capacity (196.4 mAh·g^{-1}) with a high capacity retention rate (90.7%). In short, in this study we have developed a simple strategy for dendrite-free Zn anodes. Such Zn anodes enabled highly reversible Zn plating/stripping processes. Thus, this study is expected to promote the development of metal anodes.

2 Experimental

2.1 Preparation of Zn|Sn-*X* anode

Commercial zinc foils were firstly polished to remove the surface oxide and then washed with acetone, ethanol and ultrapure water, respectively. The obtained Zn foils were immersed in different concentrations (0.01, 0.05, 0.1 and 0.2 M) of SnCl$_4$ aqueous solutions for 5 min. Subsequently, the immersed Zn foils were washed with ultrapure water several times. Finally, the Zn|Sn-*X* (*X* = 0.01, 0.05, 0.1 and 0.2 M) were obtained after rapid drying.

2.2 Preparation of iodine cathode

8 mL of phytic acid (50 wt.%) was added to 12 mL of ultrapure water and stirred in an ice water bath at about 4 °C. Subsequently, 5 mL of aniline monomer was slowly added dropwise to the above solution. 0.96 g of ammonium persulfate (APS) was dissolved in 5 mL of ultrapure water. The APS solution was transferred to the previous solution under stirring and kept overnight at about 4 °C. After the polymerization was completed, excess phytic acid was carefully washed away by ultrapure water. Finally, the obtained sample was freeze-dried and annealed at 1,000 °C for 2 h. The obtained black product was denoted as PCM-NP (porous carbon material co-doped with N and P).

2.3 Loading of iodine on PCM-NP cathode

Iodine was loaded onto the PCM-NP cathode by a simple steam method. The obtained PCM-NP (60 mg) and iodine (20 mg) were thoroughly mixed in a mass ratio of 3:1 and added into a 20 mL glass bottle. Then, the iodine-loaded PCM-NP material was obtained after keeping in an oven at 120 °C for 6 h. The areal mass loading for each PCM-NP electrode is about 6 mg·cm^{-2}.

2.4 Materials characterization

Scanning electron microscope (SEM, Gemini SEM, Carl Zeiss Microscopy GmbH) was used to characterize the morphologies of the samples at 3.0 kV. The crystallinity of samples was analyzed using a Rigaku Dmax X-ray diffractometer (XRD) under Ni filtered Cu Kα radiation. N$_2$ adsorption–desorption

isotherms and Brunauer–Emmett–Teller (BET) surface area of the sample were measured by a Kubo-X1000 instrument at 77 K. The pore size distribution was obtained by density functional theory (DFT) method.

2.5 Electrochemical measurements

For symmetrical cells, the bare Zn and Zn|Sn-*X* were used as both anode and cathode of CR2032 type coin cells. Galvanostatic charge/discharge curves and the rate performance were measured by a Neware battery test system under different current densities. Cyclic voltammetry (CV) and Tafel plots were tested on a CHI 760E electrochemical workstation. Measurements of electrochemical impedance spectroscopy (EIS) were conducted using an electrochemical workstation (Autolab) in the frequency range of 100 kHz–10 mHz. For the Zn-I$_2$ full batteries, iodine cathodes were prepared by mixing the active material, acetylene black and polytetrafluoroethylene (PTFE) with a mass ratio of 7:2:1. The electrolyte used in all the above tests was 2.0 M ZnSO$_4$ aqueous solution.

3 Results and discussion

To address the irreversible redox of Zn and the possible growth of Zn dendrites due to the so-called "tip effect" [34], Sn is coated on Zn surface with control via spontaneous galvanic replacement reaction (2Zn + SnCl$_4$ → Sn + 2ZnCl$_2$) due to the large potential gaps between Zn/Zn^{2+} and Sn/Sn^{4+} (Fig. 1(a)). The Sn coated Zn (Zn|Sn) anode is able to induce the uniform deposition of Zn via the pre-deposition effect of Sn particles, thus suppressing the growth of Zn dendrites during cycling process (Fig. 1(b)). In contrast, during the Zn plating/stripping, Zn atoms stack on the surface of bare Zn and continuously exacerbate the dendrite growth due to the tipping effect. Compared with the bare Zn, the SEM image exhibits that the Zn|Sn anode is covered with Sn crystalline grains with a size of 1–2 μm, which would provide abundant nucleation sites for Zn deposition and reduce the overpotential (Figs. 1(c) and 1(d)). Notably, the size of Sn particles (Fig. S1 in the Electronic Supplementary Material (ESM)) on the Zn surface is gradually increasing with the increasing concentration of tin ions.
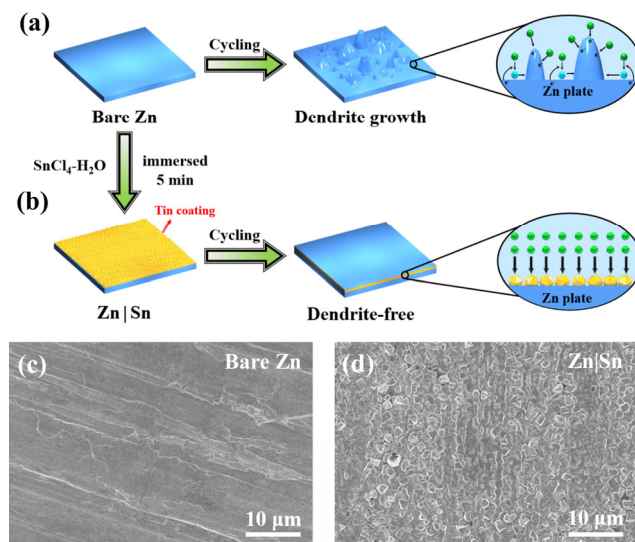

Figure 1 Schematic illustrations of the Zn|Sn anode fabrication process and the behavior of (a) bare Zn and (b) Zn|Sn during cycling. SEM images of (c) bare Zn and (d) Zn|Sn.

Finally, the Sn particles transform into large whiskers at the maximum concentration of 0.20 M (Fig. S1(d) in the ESM). The element mapping images also illustrate that the signal of Sn element is gradually enhanced with the increasing of tin ion concentration (Fig. S2 in the ESM). However, the excessive growth results in the deformation of Sn grains and the formation of dendritic surface, which is obviously not favorable to the uniform Zn deposition. In addition, the thickness of the Sn coating is about 4 μm according to the SEM image and the corresponding element mapping image (Fig. S3 in the ESM). According to the cross-sectional SEM images (Fig. S4 in the ESM), the thickness of Zn|Sn-*X* anodes is decreased with decreasing concentration of the reaction solution ($SnCl_4$ solution). Obviously, the excess deposition of Sn coating layer for Zn|Sn-0.20 results in the dendritic surface (Figs. S1(d) and S4(a) in the ESM). As shown in Fig. S4(b) in the ESM, the surface of Zn|Sn-0.10 electrode is covered by a uniform Sn coating with a thickness of around 4.2 μm. Zn|Sn-0.05 electrode has a thinner coating (2.5 μm) due to the lower Sn^{4+} concentration (Fig. S4(c) in the ESM). For the Zn|Sn-0.01 anode, no obvious interlayer interface is even observed due to the thin Sn coating layer (Fig. S4(d) in the ESM).

The surface crystallinity of samples was analyzed using XRD. As shown in Fig. 2(a), the typical XRD patterns are indexed into the characteristic peaks of Sn (PDF# 04-0673) and Zn, confirming Sn coating on Zn by spontaneous galvanic replacement reaction. The exchange current densities (i_0) of the samples were measured by Tafel curves, reflecting the kinetic parameters of the Zn plating/stripping process. As shown in Fig. 2(b), the exchange current densities of Zn|Sn-*X* are significantly higher than that of bare Zn by an order of magnitude, suggesting the faster reaction kinetics [32, 35]. The abundant nucleation sites on the surface of Sn coating are favorable for the nucleation and growth of Zn. The impedances of bare Zn and Zn|Sn-*X* in symmetrical cells were measured by EIS. The significantly reduced charge-transfer resistance of Zn|Sn-*X* indicates that the introduction of Sn coating would accelerate efficient charge transfer process and thus enhance the kinetics of the Zn plating process (Fig. S5 in the ESM) [36, 37].

Figure 2(c) shows the detailed voltage profiles of Zn|Sn-0.10 and bare Zn symmetric cells in detail at 1 mA·cm⁻² for 1 mAh·cm⁻². Zn|Sn-0.10 delivers an extremely low overpotential (13.9 mV) during the Zn plating/stripping process compared with the bare Zn (21.4 mV), suggesting the lower polarization characteristics [38]. The abundant nucleation sites on the Sn coating would reduce the reaction overpotential, resulting in the reversible deposition and stripping on the surface of Zn|Sn anodes [34, 39]. As illustrated in Fig. S6(a) in the ESM, the rate performance of Zn|Sn is superior to the bare Zn in the current density range of 0.5–10 mA·cm⁻². The results show that Zn|Sn anode has better rate performance because of the numerous nucleation sites. Particularly, the overpotential of Zn|Sn anode is only half that of bare Zn when the current density is lower than 5 mA·cm⁻² (Fig. S6(b) in the ESM). Low reaction overpotential and superior rate performance result in highly reversible Zn plating/stripping process.

Moreover, the symmetric cells of Zn|Sn-0.05 (12.1 mV) and Zn|Sn-0.01 (12 mV) also exhibit much lower cyclic overpotentials than those with bare Zn (Fig. S7 in the ESM). To the best of our knowledge, such an ultralow reaction overpotential is very rare. More importantly, the overpotential of Zn|Sn-0.10 symmetrical cell is increased from 13.9 mV (50 h) to 18.4 mV

(800 h) with a negligible polarization growth rate within 900 h compared with Zn|Sn-0.05 symmetrical cells (22.6 mV at 800 h). Slowly increasing polarization indicates that the Zn|Sn-0.10 anode is more stable than other anodes, resulting from the uniform surface and relatively suitable size of Sn particles. The Zn|Sn-0.01 symmetrical cell shows an unstable voltage distribution and fails after 800 h which may arise from the non-efficient Sn coating layer. Due to the high adsorption energy and faster deposition kinetics of Sn coating on Zn, the unprecedented low voltage polarization is also superior to most reported Zn anodes previously with different coatings (Fig. 2(d)) [14, 22, 24, 37, 40–42].

Galvanostatic charge–discharge (GCD) curves were measured for the cycling stability of bare Zn and Zn|Sn-*X* in symmetric cells at various current densities and capacities. As expected, the cycling performance of all Zn|Sn-*X* symmetric cells is enhanced compared to the bare Zn (about 100 h). Especially, the Zn|Sn-0.10 symmetric cells with a lower overpotential exhibit a remarkable cycle stability with over 900 h at a current density of 1 mA·cm⁻² for 1 mAh·cm⁻² (Fig. 2(e)). The lifespan of the Zn|Sn-0.10 electrode is extended to nearly ten times higher than that of the bare Zn electrode, which would be attributed to the reversible deposition of Zn caused by the Sn coating and the induced deposition effect to prevent dendrites growth. Even at high current density of 5 mA·cm⁻², the Zn|Sn-*X* symmetrical cells indicate a long lifespan up to 600 h, six times longer than that of the bare Zn one (Fig. S8 in the ESM). The symmetrical cells with Zn|Sn-*X* electrodes depict 36 and
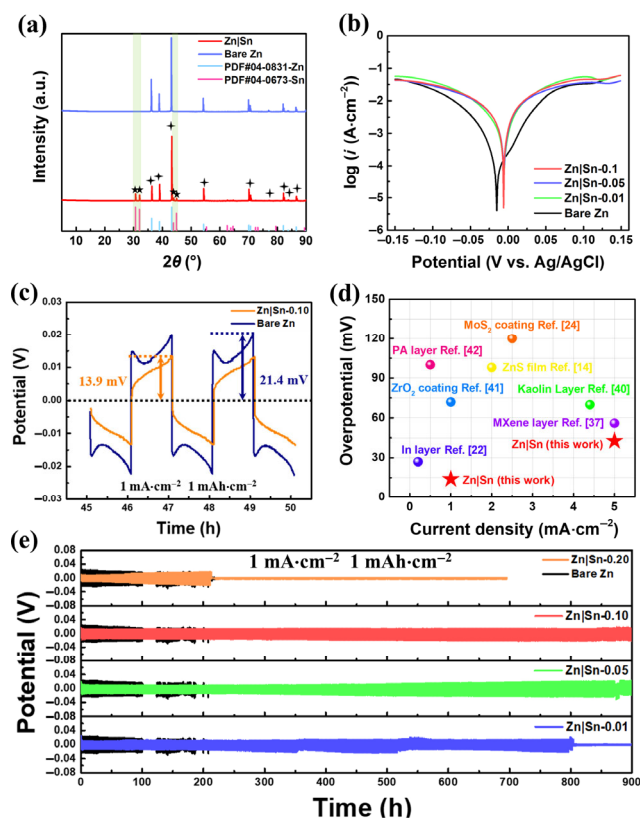

Figure 2 (a) XRD patterns of bare Zn and Zn|Sn. (b) Tafel curves of bare Zn and Zn|Sn-*X* in 2 M $ZnSO_4$ electrolyte aqueous solution. (c) Detailed voltage profiles of Zn|Sn-0.10 and bare Zn symmetric cells. (d) Comparison of overpotential between Zn|Sn and Zn anodes reported in the literature. (e) Cycling performance of bare Zn and Zn|Sn-*X* in symmetric cells at 1 mA·cm⁻² for 1 mAh·cm⁻².

38 mV in the initial polarization and 50 h voltage hysteresis, respectively, which is significantly lower than that of the cell with bare Zn anode (55 and 61 mV). Obviously, the greatly extended cycling lifespan is benefited from the reversible Zn plating/stripping process enabled by the induced deposition effect of the Sn coating.

The above-discussed results suggest that the excellent deposition kinetics of Zn|Sn-*X* electrodes would be benefited by the favourable Zn nucleation due to the Sn coating on the surface (Fig. 3(a)). The total Gibbs free energy change (ΔG) is the sum of the free energy change of bulk surface (ΔG_B) and the free energy change of the hemispherical crystal nucleus, which can be calculated according to the following equation [43]

$$\Delta G = \Delta G_S + \Delta G_B = \pi r^2 \sigma - \frac{2}{3}\pi r^3 \frac{nF\eta}{V_m} \quad (1)$$

where *r* is the crystal nucleus radius; σ is the surface free energy, and V_m is the molar volume [43]. As shown in Fig. 3(b), the free energy gradually increases to the maximal value when the crystal nucleus is smaller than the critical radius, and then decreases during the growth process. Notably, the initial formation of the crystal nucleus is quite difficult due to the increased free energy [43, 44]. However, the decreasing free energy suggests the deposition is a spontaneous process when the crystal nucleus is larger than the critical radius. Therefore, the pre-coating of Sn nanoparticles with suitable sizes would reduce the nucleation barrier of Zn by adjusting the growth process. Thus, the Zn|Sn-0.10 electrode exhibits the optimal redox process among all the Zn|Sn-*X* electrodes because of the suitable particle size. The nucleation overpotentials of the Zn|Sn-*X* anodes and the bare Zn electrode were evaluated at a current density of 1 mA·cm^{-2} with a capacity of 1 mAh·cm^{-2} (Fig. 3(c)). As expected, the nucleation overpotential is obviously reduced due to the contribution of the Sn coating. Especially, the Zn|Sn-0.10 electrode exhibits a negligible nucleation overpotential of only 1 mV. In contrast, the bare Zn electrode exhibits a higher nucleation overpotential (~ 22 mV), indicating a higher nucleation barrier on the surface of bare Zn. The

results demonstrate that the Sn coating greatly reduces the nucleation overpotential for the favorable Zn deposition.

Figure 4 reveals the changes in the surface morphology and electrochemical performance of bare Zn and Zn|Sn-0.10 before and after cycling tests. As shown in Fig. 4(a), the non-uniform deposition of zinc on the surface of bare Zn would cause the dendrites growth and the growth of dendrites intensifies with the increasing number of cycles. In contrast, the surface of the Zn|Sn anode is not distorted with increasing cycle numbers for 50 h (Fig. 4(b)). The SEM images show that the gradual dendrite growth on the surface of bare Zn would possibly pierce the separator and cause battery failure (Figs. 4(c)–4(e), and Fig. S9 in the ESM) [45]. Due to the induced deposition effect of the Sn particles, Zn atoms are directionally deposited around the Sn particles to form a flat deposition layer. The surface roughness of Zn|Sn anode decreases continuously during cycling and the Zn|Sn anode finally transforms into a sandwich structure (Figs. 4(f)–4(h), and Fig. S10 in the ESM). The SEM images exhibit that the uniform Zn without dendrites is successfully formed on the surface of Zn|Sn anode, which is consistent with the results of the cycling performance above. We have shown that Sn particles can induce uniform deposition of Zn and effectively prevent the growth of dendrites due to the favorable nucleus process and the high adsorption energy for Zn.

As shown in Fig. 4(i), the peak intensity of Sn in XRD pattern of Zn|Sn cycled for 50 h is lower in comparison with the Zn|Sn
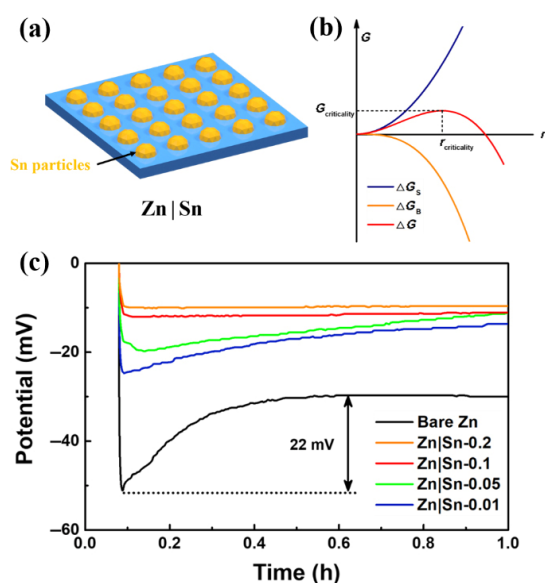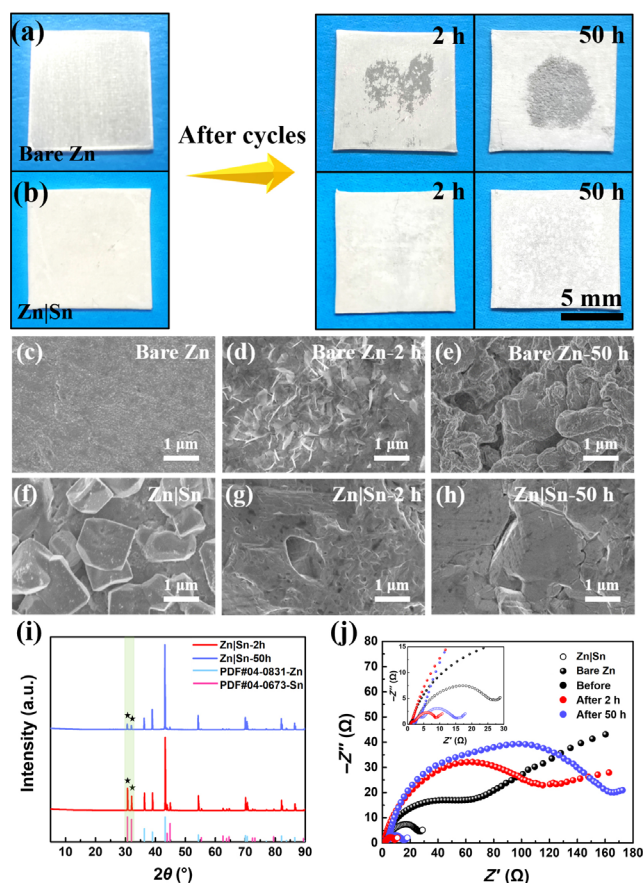

Figure 3 (a) Schematic diagram of Sn crystal nuclei on the Zn|Sn anode. (b) Free energy change of the proposed nucleation during Zn plating process. (c) Nucleation overpotentials of Zn|Sn-*X* and the bare Zn electrode at a current density of 1 mA·cm^{-2}.

Figure 4 Optical photographs of bare Zn (a) and Zn|Sn (b) before and after 50 h. SEM images of bare Zn ((c)–(e)) and Zn|Sn ((f)–(h)) before and after cycles at 1 mA·cm^{-2} for 1 mAh·cm^{-2}. (i) XRD patterns of Zn|Sn after cycles. (j) EIS of bare Zn and Zn|Sn before and after cycles in symmetric cells.

cycled for 2 h. Such changes indicate the transformation into a sandwich structure gradually. In addition, no characteristic peaks of the corrosion products (e.g., $Zn_4SO_4(OH)_6 \cdot 3H_2O$) are found, indicating the suppressed corrosion reaction. EIS was used to study the change of the impedance in the symmetrical cells after cycling processes. According to EIS results, the charge-transfer resistance of bare Zn becomes larger with increasing cycle number. In contrast, the charge-transfer resistance of Zn|Sn is decreased dramatically from 23.9 to 6.8 Ω after the first cycle (Fig. 4(j)). The changes on charge-transfer resistance would be attributed to the transformation from the double-layer structure to the sandwich structure. Compared with the double-layer structure, Zn ions do not need to pass through the Sn layer during the stripping on the sandwich structure. Subsequently, the resistance of the symmetric cell of Zn|Sn increases from 6.8 to 11.2 Ω after 50 h of cycling test. The EIS results strongly suggest that a structural transformation occurs after the first cycle, which is in good agreement with the results of XRD and SEM.

The Zn|Sn anode was assembled with the iodine-loaded porous carbon electrode (Figs. S11–S15 in the ESM) as a Zn-I_2 battery for further electrochemical testing (Fig. 5). For the bare Zn and Zn|Sn anodes, the CV curves exhibit a similar shape, suggesting no negative effect on the redox kinetics of iodine (Fig. 5(a)). Furthermore, only a pair of redox peaks without other impurity peaks in the voltage range of 0.6–1.6 V indicate that the Sn layer on the surface of the Zn|Sn anode remains stable throughout the operating potential [41].

The specific capacity of the Zn-I_2 battery was calculated on the basis of the theoretical capacity of iodine (211 mAh·g^{-1}) and its mass loading. The rate performance of Zn|Sn-I_2 batteries and Zn-I_2 batteries were evaluated from 1 to 10 C, respectively. As illustrated in Fig. 5(b), Zn-I_2 batteries assembled with bare Zn (212.2 mAh·g^{-1}) and Zn|Sn anode (223.5 mAh·g^{-1}) both show a similar initial capacity at 1 C. Notably, the capacitive contribution of porous carbon support would also contribute to the specific capacity slightly [46, 47]. However, the specific capacity of the Zn-I_2 batteries drops sharply in the subsequent cycles, which is caused by the slow reaction kinetics of the

Zn anode. The battery with Zn|Sn anode exhibits better rate performance with increasing current density. Especially, the Zn|Sn-I_2 batteries exhibit a stable capacity in the test and maintain a high specific capacity of 167 mAh·g^{-1} even at a high current density of 10 C, which is much higher than that of the Zn-I_2 batteries (142 mAh·g^{-1}). When the current density returns to the initial 1 C after 80 cycles, the Zn|Sn-I_2 batteries still show a specific capacity as high as 216.7 mAh·g^{-1} with a high capacity retention (96.8%). In contrast, even if the current density is restored to 0.5 C, the Zn-I_2 battery cannot recover to its initial specific capacity. The normal charge/discharge curves also indicate good rate performance of Zn|Sn-I_2 batteries, owning to the fast deposition kinetics of the Zn|Sn anodes (Fig. 5(c)). Cycling performance and coulombic efficiency of Zn–I_2 batteries were further evaluated at 5 C. As shown in Fig. 5(d), Zn|Sn-I_2 batteries show a high specific capacity (196.4 mAh·g^{-1}) and excellent stability with a high capacity retention (90.7%) after 1,200 cycles. The good cycling stability and high capacity retention of Zn|Sn-I_2 batteries come from the high reversibility and stability of the dendrite-free Zn|Sn anode. However, the Zn-I_2 batteries assembled with bare Zn lose its specific capacity rapidly and only have a capacity retention rate of 81.6%. Compared with Zn-I_2 batteries, the greatly reduced charge transfer resistance shows the favorable reaction kinetics of Zn|Sn-I_2 batteries with good conductivity (Fig. 5(e)). Interestingly, two Zn|Sn-I_2 button batteries connected in series successfully drive a small commercial fan (Fig. S16 in the ESM). The results prove the good electrochemical performance and improved stability of Zn|Sn anodes.

4 Conclusions

In conclusion, a simple and effective strategy was developed to construct highly reversible dendrite-free Zn anodes for Zn-I_2 batteries via the spontaneous formation of tin coating. The Sn coating layer has the unique characteristics of high adsorption energy for Zn, inherent chemical inertness which enables favorable deposition kinetics and improved stability. Zn atoms will be preferentially deposited on the Sn coating instead of
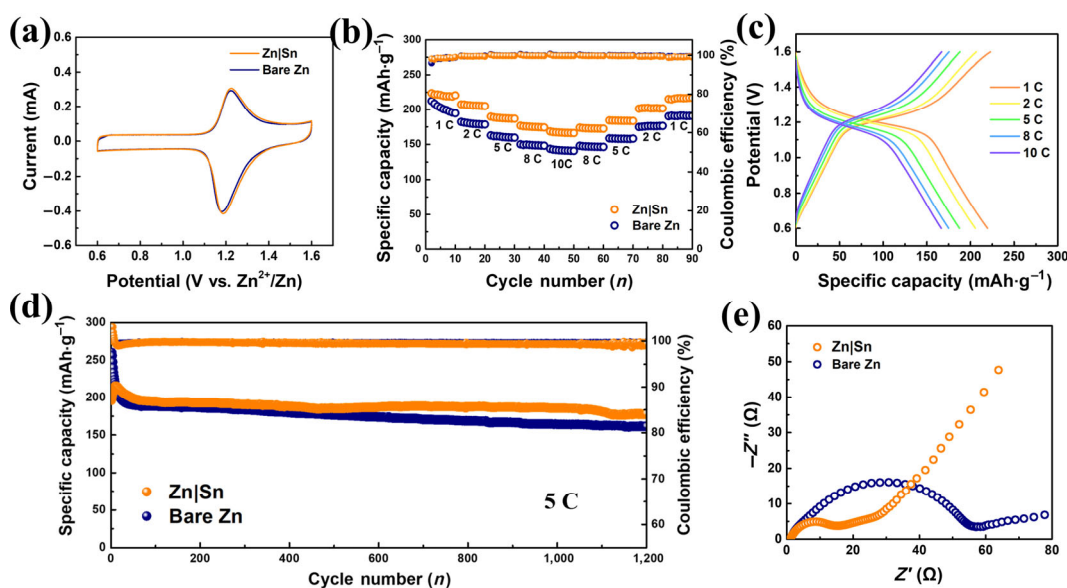

Figure 5 Comparison of electrochemical performance of Zn|Sn and bare Zn in Zn-I_2 batteries. (a) CV curves at 0.1 mV·s^{-1}. (b) Rate performance of Zn|Sn-I_2 batteries and Zn-I_2 batteries. (c) Corresponding charge/discharge curves under different current densities. (d) Cycling performance and Coulombic efficiency at 5 C. (e) EIS of Zn|Sn-I_2 batteries and Zn-I_2 batteries.

accumulating on the interface and eventually forming Zn dendrites due to the high zinc affinity of the Sn layer. Therefore, the Zn|Sn anode can achieve high reversibility during Zn plating/stripping by the induced deposition effect. As expected, the Zn|Sn anodes maintain over 900 h of plating/stripping cycles in symmetrical cells with a rare low overpotential (13.9 mV) compared to the bare Zn (21.4 mV). Zn|Sn-I$_2$ batteries assembled with Zn|Sn anode and iodine cathode exhibit a remarkable stability during 1,200 cycles with a high capacity retention (90.7%). This work demonstrates a simple and universal strategy to fundamentally inhibit the formation of Zn dendrites, which can be extended to other metal anodes for the development of advanced metal anodes.

Acknowledgements

Electronic Supplementary Material: Supplementary material (SEM images, XRD patterns, N$_2$ adsorption–desorption isotherms and supporting electrochemical measurement) is available in the online version of this article at https://doi.org/10.26599/NRE.2022.9120025.

Declaration of conflicting interests

The authors declare no conflicting interests regarding the content of this article.

References

[1] Zhang, S. L.; Sun, L.; Fan, Q. N.; Zhang, F. L.; Wang, Z. J.; Zou, J. S.; Zhao, S. Y.; Mao, J. F.; Guo, Z. P. Challenges and prospects of lithium-CO$_2$ batteries. *Nano Res. Energy* **2022**, *1*, e9120001.

[2] Lv, C. D.; Zhou, X.; Zhong, L. X.; Yan, C. S.; Srinivasan, M.; Seh, Z. W.; Liu, C. T.; Pan, H. G.; Li, S. Z.; Wen, Y. G. et al. Machine learning: An advanced platform for materials development and state prediction in lithium-ion batteries. *Adv. Mater.* **2021**, *34*, 2101474.

[3] Yan, C. S.; Lv, C. D.; Jia, B. E.; Zhong, L. X.; Cao, X.; Guo, X. L.; Liu, H. J.; Xu, W. J.; Liu, D. B.; Yang, L. et al. Reversible Al metal anodes enabled by amorphization for aqueous aluminum batteries. *J. Am. Chem. Soc.* **2022**, *144*, 11444–11455.

[4] Zeng, X. H.; Liu, J. T.; Mao, J. F.; Hao, J. N.; Wang, Z. J.; Zhou, S.; Ling, C. D.; Guo, Z. P. Toward a reversible Mn^{4+}/Mn^{2+} redox reaction and dendrite-free Zn anode in near-neutral aqueous Zn/MnO$_2$ batteries via salt anion chemistry. *Adv. Energy Mater.* **2020**, *10*, 1904163.

[5] Wang, G.; Kohn, B.; Scheler, U.; Wang, F. X.; Oswald, S.; Löffler, M.; Tan, D. M.; Zhang, P. P.; Zhang, J.; Feng, X. L. A high-voltage, dendrite-free, and durable Zn-graphite battery. *Adv. Mater.* **2020**, *32*, 1905681.

[6] Wu, Y. Z.; Wang, M. C.; Tao, Y.; Zhang, K.; Cai, M. L.; Ding, Y.; Liu, X. P.; Hayat, T.; Alsaedi, A.; Dai, S. Y. Electrochemically derived graphene-like carbon film as a superb substrate for high-performance aqueous Zn-ion batteries. *Adv. Funct. Mater.* **2020**, *30*, 1907120.

[7] Zou, Y. P.; Liu, T. T.; Du, Q. J.; Li, Y. Y.; Yi, H. B.; Zhou, X.; Li, Z.

X.; Gao, L. J.; Zhang, L.; Liang, X. A four-electron Zn-I$_2$ aqueous battery enabled by reversible I$^-$/I$_2$/I$^+$ conversion. *Nat. Commun.* **2021**, *12*, 170.

[8] Naveed, A.; Yang, H. J.; Shao, Y. Y.; Yang, J.; Yanna, N.; Liu, J.; Shi, S. Q.; Zhang, L. W.; Ye, A. J.; He, B. et al. A highly reversible Zn anode with intrinsically safe organic electrolyte for long-cycle-life batteries. *Adv. Mater.* **2019**, *31*, 1900668.

[9] Wang, Z.; Huang, J. H.; Guo, Z. W.; Dong, X. L.; Liu, Y.; Wang, Y. G.; Xia, Y. Y. A metal-organic framework host for highly reversible dendrite-free zinc metal anodes. *Joule* **2019**, *3*, 1289–1300.

[10] Yang, H. J.; Qiao, Y.; Chang, Z.; Deng, H.; He, P.; Zhou, H. S. A metal-organic framework as a multifunctional ionic sieve membrane for long-life aqueous zinc-iodide batteries. *Adv. Mater.* **2020**, *32*, 2004240.

[11] Wang, F. X.; Tseng, J.; Liu, Z. C.; Zhang, P. P.; Wang, G.; Chen, G. B.; Wu, W. X.; Yu, M. H.; Wu, Y. P.; Feng, X. L. A stimulus-responsive zinc-iodine battery with smart overcharge self-protection function. *Adv. Mater.* **2020**, *32*, 2000287.

[12] Naveed, A.; Yang, H. J.; Yang, J.; Nuli, Y.; Wang, J. L. Highly reversible and rechargeable safe Zn batteries based on a triethyl phosphate electrolyte. *Angew. Chem., Int. Ed.* **2019**, *58*, 2760–2764.

[13] Ma, L. T.; Chen, S. M.; Li, N.; Liu, Z. X.; Tang, Z. J.; Zapien, J. A.; Chen, S. M.; Fan, J.; Zhi, C. Y. Hydrogen-free and dendrite-free all-solid-state Zn-Ion batteries. *Adv. Mater.* **2020**, *32*, 1908121.

[14] Hao, J. N.; Li, B.; Li, X. L.; Zeng, X. H.; Zhang, S. L.; Yang, F. H.; Liu, S. L.; Li, D.; Wu, C.; Guo, Z. P. An in-depth study of Zn metal surface chemistry for advanced aqueous Zn-ion batteries. *Adv. Mater.* **2020**, *32*, 2003021.

[15] Wang, Z. Q.; Zhou, M.; Qin, L. P.; Chen, M. H.; Chen, Z. X.; Guo, S.; Wang, L. B.; Fang, G. Z.; Liang, S. Q. Simultaneous regulation of cations and anions in an electrolyte for high-capacity, high-stability aqueous zinc-vanadium batteries. *eScience* **2022**, *2*, 209–218.

[16] Cao, L. S.; Li, D.; Deng, T.; Li, Q.; Wang, C. S. Hydrophobic organic-electrolyte-protected zinc anodes for aqueous zinc batteries. *Angew. Chem., Int. Ed.* **2020**, *59*, 19292–19296.

[17] Wang, M. M.; Meng, Y. H.; Li, K.; Ahmad, T.; Chen, N.; Xu, Y.; Sun, J. F.; Chuai, M. Y.; Zheng, X. H.; Yuan, Y. et al. Toward dendrite-free and anti-corrosion Zn anodes by regulating a bismuth-based energizer. *eScience*, in press, https://doi.org/10.1016/j.esci.2022.04.003.

[18] Jin, S.; Yin, J. F.; Gao, X. S.; Sharma, A.; Chen, P. Y.; Hong, S. F.; Zhao, Q.; Zheng, J. X.; Deng, Y.; Joo, Y. L. et al. Production of fast-charge Zn-based aqueous batteries via interfacial adsorption of ion-oligomer complexes. *Nat. Commun.* **2022**, *13*, 2283.

[19] Cao, Z. Y.; Zhu, X. D.; Xu, D. X.; Dong, P.; Chee, M. O. L.; Li, X. J.; Zhu, K. Y.; Ye, M. X.; Shen, J. F. Eliminating Zn dendrites by commercial cyanoacrylate adhesive for zinc ion battery. *Energy Storage Mater.* **2021**, *36*, 132–138.

[20] Zhao, R. R.; Yang, Y.; Liu, G. X.; Zhu, R. J.; Huang, J. B.; Chen, Z. Y.; Gao, Z. H.; Chen, X.; Qie, L. Redirected Zn electrodeposition by an anti-corrosion elastic constraint for highly reversible Zn anodes. *Adv. Funct. Mater.* **2021**, *31*, 2001867.

[21] Yan, M. D.; Xu, C. L.; Sun, Y.; Pan, H. L.; Li, H. Manipulating Zn anode reactions through salt anion involving hydrogen bonding network in aqueous electrolytes with PEO additive. *Nano Energy.* **2021**, *82*, 105739.

[22] Han, D. L.; Wu, S. C.; Zhang, S. W.; Deng, Y. Q.; Cui, C. J.; Zhang, L. N.; Long, Y.; Li, H.; Tao, Y.; Weng, Z. et al. A corrosion-resistant and dendrite-free zinc metal anode in aqueous systems. *Small* **2020**, *16*, 2001736.

[23] He, P.; Huang, J. X. Chemical passivation stabilizes Zn anode. *Adv. Mater.* **2022**, *34*, 2109872.

[24] Bhoyate, S.; Mhin, S.; Jeon, J. E.; Park, K.; Kim, J.; Choi, W. Stable and high-energy-density Zn-ion rechargeable batteries based on a MoS$_2$-coated Zn anode. *ACS Appl. Mater. Interfaces* **2020**, *12*, 27249–27257.

[25] Zhang, X. T.; Li, J. X.; Liu, D. Y.; Liu, M. K.; Zhou, T. S.; Qi, K. W.; Shi, L.; Zhu, Y. C.; Qian, Y. T. Ultra-long-life and highly reversible Zn metal anodes enabled by a desolvation and deanionization interface layer dagger. *Energy Environ. Sci.* **2021**, *14*, 3120–3129.

[26] Zheng, J. X.; Bock, D. C.; Tang, T.; Zhao, Q.; Yin, J. F.; Tallman, K. R.; Wheeler, G.; Liu, X. T.; Deng, Y.; Jin, S. et al. Regulating electrodeposition morphology in high-capacity aluminium and zinc battery anodes using interfacial metal-substrate bonding. *Nat. Energy* **2021**, *6*, 398–406.

[27] Wu, T. H.; Zhang, Y.; Althouse, Z. D.; Liu, N. Nanoscale design of zinc anodes for high-energy aqueous rechargeable batteries. *Mater. Today Nano* **2019**, *6*, 100032.

[28] Shi, J. Q.; Sun, T. J.; Bao, J. Q.; Zheng, S. B.; Du, H. H.; Li, L.; Yuan, X. M.; Ma, T.; Tao, Z. L. "Water-in-deep eutectic solvent" electrolytes for high-performance aqueous Zn-ion batteries. *Adv. Funct. Mater.* **2021**, *31*, 2102035.

[29] Wang, F.; Borodin, O.; Gao, T.; Fan, X. L.; Sun, W.; Han, F. D.; Faraone, A.; Dura, J. A.; Xu, K.; Wang, C. S. Highly reversible zinc metal anode for aqueous batteries. *Nat. Mater.* **2018**, *17*, 543–549.

[30] Zeng, X. H.; Mao, J. F.; Hao, J. N.; Liu, J. T.; Liu, S. L.; Wang, Z. J.; Wang, Y. Y.; Zhang, S. L.; Zheng, T.; Liu, J. W. et al. Electrolyte design for *in situ* construction of highly Zn^{2+}-conductive solid electrolyte interphase to enable high-performance aqueous Zn-ion batteries under practical conditions. *Adv. Mater.* **2021**, *33*, 2007416.

[31] Cao, L. S.; Li, D.; Hu, E. Y.; Xu, J. J.; Deng, T.; Ma, L.; Wang, Y.; Yang, X. Q.; Wang, C. S. Solvation structure design for aqueous Zn metal batteries. *J. Am. Chem. Soc.* **2020**, *142*, 21404–21409.

[32] Li, S. Y.; Fu, J.; Miao, G. X.; Wang, S. P.; Zhao, W. Y.; Wu, Z. C.; Zhang, Y. J.; Yang, X. W. Toward planar and dendrite-free Zn electrodepositions by regulating Sn-crystal textured surface. *Adv. Mater.* **2021**, *33*, 2008424.

[33] Yin, Y. B.; Wang, S. N.; Zhang, Q.; Song, Y.; Chang, N. N.; Pan, Y. W.; Zhang, H. M.; Li, X. F. Dendrite-free zinc deposition induced by tin-modified multifunctional 3D host for stable zinc-based flow battery. *Adv. Mater.* **2020**, *32*, 1906803.

[34] Xie, F. X.; Li, H.; Wang, X. S.; Zhi, X.; Chao, D. L.; Davey, K.; Qiao, S. Z. Mechanism for zincophilic sites on zinc-metal anode hosts in aqueous batteries. *Adv. Energy Mater.* **2021**, *11*, 2003419.

[35] Tu, Z. Y.; Choudhury, S.; Zachman, M. J.; Wei, S. Y.; Zhang, K. H.; Kourkoutis, L. F.; Archer, L. A. Fast ion transport at solid–solid interfaces in hybrid battery anodes. *Nat. Energy* **2018**, *3*, 310–316.

[36] Cao, P. H.; Zhou, X. Y.; Wei, A. R.; Meng, Q.; Ye, H.; Liu, W. P.; Tang, J. J.; Yang, J. Fast-charging and ultrahigh-capacity zinc metal anode for high-performance aqueous zinc-ion batteries. *Adv. Funct. Mater.* **2021**, *31*, 2100398.

[37] Zhang, N. N.; Huang, S.; Yuan, Z. S.; Zhu, J. C.; Zhao, Z. F.; Niu, Z. Q. Direct self-assembly of MXene on Zn anodes for dendrite-free aqueous Zinc-Ion batteries. *Angew. Chem., Int. Ed.* **2021**, *60*, 2861–2865.

[38] Jin, Y.; Han, K. S.; Shao, Y. Y.; Sushko, M. L.; Xiao, J.; Pan, H. L.; Liu, J. Stabilizing zinc anode reactions by polyethylene oxide polymer in mild aqueous electrolytes. *Adv. Funct. Mater.* **2020**, *30*, 2003932.

[39] Xu, X. L.; Chen, Y.; Zheng, D.; Ruan, P. C.; Cai, Y. H.; Dai, X. J.; Niu, X. X.; Pei, C. J.; Shi, W. H.; Liu, W. X. et al. Ultra-fast and scalable saline immersion strategy enabling uniform zn nucleation and deposition for high-performance Zn-ion batteries. *Small.* **2021**, *17*, 2101901.

[40] Deng, C. B.; Xie, X. S.; Han, J. W.; Tang, Y.; Gao, J. W.; Liu, C. X.; Shi, X. D.; Zhou, J.; Liang, S. Q. A sieve-functional and uniform-porous kaolin layer toward stable zinc metal anode. *Adv. Funct. Mater.* **2020**, *30*, 2000599.

[41] Liang, P. C.; Yi, J.; Liu, X. Y.; Wu, K.; Wang, Z.; Cui, J.; Liu, Y. Y.; Wang, Y. G.; Xia, Y. Y.; Zhang, J. J. Highly reversible Zn anode enabled by controllable formation of nucleation sites for Zn-based batteries. *Adv. Funct. Mater.* **2020**, *30*, 1908528.

[42] Zhao, Z. M.; Zhao, J. W.; Hu, Z. L.; Li, J. D.; Li, J. J.; Zhang, Y. J.; Wang, C.; Cui, G. L. Long-life and deeply rechargeable aqueous Zn anodes enabled by a multifunctional brightener-inspired interphase. *Energy Environ. Sci.* **2019**, *12*, 1938–1949.

[43] Pei, A.; Zheng, G. Y.; Shi, F. F.; Li, Y. Z.; Cui, Y. Nanoscale nucleation and growth of electrodeposited lithium metal. *Nano Lett.* **2017**, *17*, 1132–1139.

[44] Zou, P. C.; Sui, Y. M.; Zhan, H. C.; Wang, C. Y.; Xin, H. L.; Cheng, H. M.; Kang, F. Y.; Yang, C. Polymorph evolution mechanisms and regulation strategies of lithium metal anode under multiphysical fields. *Chem. Rev.* **2021**, *121*, 5986–6056.

[45] Yuan, D.; Zhao, J.; Ren, H.; Chen, Y. Q.; Chua, R.; Jie, E. T. J.; Cai, Y.; Edison, E.; Manalastas, W. Jr.; Wong, M. W. et al. Anion texturing towards dendrite-free Zn anode for aqueous rechargeable batteries. *Angew. Chem., Int. Ed.* **2021**, *60*, 7213–7219.

[46] Ma, J. Z.; Liu, M. M.; He, Y. L.; Zhang, J. T. Iodine redox chemistry in rechargeable batteries. *Angew. Chem., Int. Ed.* **2021**, *60*, 12636–12647.

[47] Chen, S.; Chen, Q. W.; Ma, J. Z.; Wang, J. J.; Hui, K. S.; Zhang, J. T. Interface coordination stabilizing reversible redox of zinc for high-performance zinc-iodine batteries. *Small.* **2022**, *18*, 2200168.

Tian Yadong is currently a master degree candidate at Shandong University, Jinan, China. His research direction is focused on the new generation of energy storage conversion devices, such as Zn-I$_2$ batteries.

Prof. Jintao Zhang obtained his PhD degree from the Department of Chemical and Biomolecular Engineering at the University of Singapore in 2012. He was a postdoctoral fellow at Nanyang Technological University (Singapore) and Case Western Reserve University (USA). In fall 2015, he joined the School of Chemistry and Chemical Engineering, Shandong University as a full professor. His research interests include the rational design and synthesis of advanced materials for electrocatalysis, electrochemical energy storage, and conversion (e.g., Zn-air battery, halogen-based batteries, fuel cells, and supercapacitors).